

Experimental validation of a transport-based imaging method in highly scattering environments

Guillaume Bal* Lawrence Carin[†] Dehong Liu[‡] Kui Ren[§]

May 1, 2007

Abstract

We demonstrate the effectiveness of a transport-based reconstruction method for imaging in highly scattering environments. Experimentally measured wave energy data are used to reconstruct extended inclusions buried in scattering media or hidden behind non-penetrable obstacles. The performance of the imaging method is illustrated under various circumstances, via a set of electromagnetic experiments.

Key words. Imaging in random media, electromagnetic wave propagation, radiative transport equation, inverse transport problems, incoherent-imaging,

1 Introduction

Imaging extended objects in random media using acoustic or electromagnetic measurements has received considerable attention in the recent years [2, 6, 10, 11, 15]. Depending on the strength of multiple scattering in the media, different methods have been proposed to address the imaging problem [7, 8, 9, 12, 14, 22]. These methods are based on measurements of the coherent wave field, i.e., measurements of both the amplitude and the phase of the wave fields. Phase information is crucial in all of the above methods. It can be used in two situations: (i) when the medium is weakly scattering, and (ii) when the medium is strongly scattering and *known exactly*. When the medium is strongly scattering and not known exactly, the phase information is all but random and thus cannot be used efficiently for imaging purposes.

The alternative to a coherent-measurement approach is incoherent-measurement imaging. In such instances, however, we need a model for the incoherent wave fields,

*Department of Applied Physics & Applied Mathematics, Columbia University, New York, NY 10027; gb2030@columbia.edu; <http://www.columbia.edu/~gb2030>

[†]Department of Electrical and Computer Engineering, Duke University, Durham, NC 27708; lcarin@ee.duke.edu

[‡]Department of Electrical and Computer Engineering, Duke University, Durham, NC 27708; liudh@ee.duke.edu

[§]Department of Applied Physics & Applied Mathematics, Columbia University, New York, NY 10027; kr2002@columbia.edu; <http://www.columbia.edu/~kr2002>

or equivalently for the wave energy density. One of the simplest models for the wave energy density, which works in the presence of moderately scattering media, is radiative transport. A transport-based imaging framework was proposed in [4, 5] to consider media where multiple scattering effects are dominant. Instead of using wave field measurements, which are highly sensitive to the configuration of the medium, one measures the statistically more robust wave energy density. Imaging in random media thus becomes an inverse transport problem, where the constitutive parameters in the transport equation are to be inverted from wave energy measurements on an array of detectors.

Numerical simulations based on synthetic data show the robustness of transport-based inversions [5]. The objective of this paper is to verify the applicability of the method in practical microwave settings by performing reconstructions based on experimental measurements of electromagnetic waves when the wavelength is small enough to be highly sensitive to the medium heterogeneity (this corresponding to 10 GHz in the measurements considered here).

The rest of the paper is structured as follows. After briefly introducing the radiative transport equation for wave propagation in highly scattering media, we introduce the transport-based imaging method in Section 2. In Section 3, we describe the experimental system used to perform the electromagnetic measurements. In Section 4, we perform a detailed analysis of the measured data using the transport-based imaging method. Imaging results are presented in several experimental settings. Conclusions are offered in Section 5.

2 Transport-based Reconstruction Method

2.1 Transport model for waves in random media

The imaging method proposed in this work hinges on the fact that the energy density of high frequency waves propagating in highly scattering environments can be accurately modeled by the radiative transport equation. To be more precise, we consider frequency-domain wave propagation in highly scattering media in \mathbb{R}^d ($d = 2, 3$). In our experimental setup, the geometry is described accurately by dimension $d = 2$. The heterogeneities in the medium are modeled by an index of refraction $Q(\mathbf{x})$. We assume that $Q(\mathbf{x}) = 0$ in vacuum and assumes a large value at the locations of localized scatterers.

The carrier wavenumber is here denoted by $k = \omega/c$, where ω is modulation frequency and c is wave speed in vacuum. The frequency-domain wave equation with refractive index $Q(\mathbf{x})$ is given by:

$$\Delta u + k^2 u + Q(\mathbf{x})u = \phi(\mathbf{x}) \quad \text{in } \mathbb{R}^d, \quad (1)$$

for some source term $\phi(\mathbf{x})$ and is augmented by the following radiation condition:

$$\lim_{r \rightarrow \infty} r^{\frac{d-1}{2}} \left(\frac{\partial u}{\partial r} - iku \right) = 0, \quad (2)$$

where $r = |\mathbf{x}|$.

In highly scattering regimes, the wave field $u(\mathbf{x})$ is highly oscillatory and its phase is essentially random. For imaging purposes, it is therefore advantageous to consider the

wave energy density $|u(\mathbf{x})|^2$, which is more immune to statistical fluctuations [2, 3, 6]. Unless we are in extremely highly scattering environments, in which $|u(\mathbf{x})|^2$ may be seen to solve a diffusion equation [19, 20], in general we cannot find a closed form equation for the spatial energy density. The phase-space energy density, however, is known to satisfy a radiative transfer equation [5, 19]. The phase space energy density $\Phi(\mathbf{x}, \hat{\mathbf{k}})$ measures the density of energy at position \mathbf{x} propagating with direction $\hat{\mathbf{k}}$ and we thus have that

$$|u(\mathbf{x})|^2 = \int_{S^{d-1}} \Phi(\mathbf{x}, \hat{\mathbf{k}}) d\hat{\mathbf{k}}, \quad (3)$$

where S^{d-1} is the unit sphere in \mathbb{R}^d . For monochromatic waves, the radiative transfer equation takes the form

$$c\hat{\mathbf{k}} \cdot \nabla \Phi(\mathbf{x}, \hat{\mathbf{k}}) + \Sigma(\mathbf{x})\Phi(\mathbf{x}, \hat{\mathbf{k}}) = \Sigma(\mathbf{x}) \frac{1}{|S^{d-1}|} \int_{S^{d-1}} \Phi(\mathbf{x}, \hat{\mathbf{k}}') d\hat{\mathbf{k}}' + f(\mathbf{x}), \quad (4)$$

where $|S^{d-1}|$ is the measure of the sphere S^{d-1} and the radiating source is given by [5]:

$$f(\mathbf{x}) = \frac{\omega^{d-3}}{c^{d-4}4(2\pi)^{d-1}} \delta(\mathbf{x}) |\hat{\phi}(\mathbf{k})|^2, \quad (5)$$

where $\hat{\phi}(\mathbf{k}) = \int_{\mathbb{R}^d} e^{-i\mathbf{k}\cdot\mathbf{x}} \phi(\mathbf{x}) d\mathbf{x}$ is the Fourier transform of $\phi(\mathbf{x})$. In our experimental setting, the source is modeled by $\phi(\mathbf{x}) = \delta(\mathbf{x})$ so that $\hat{\phi}(\mathbf{k}) = 1$. The main characteristic parameter in the above equation is the mean free path $c_0\Sigma^{-1}$. A large mean free path corresponds to a weakly scattering medium, while a small mean free path corresponds to a strongly scattering medium. We have assumed that scattering is isotropic so that Σ^{-1} is independent of $\hat{\mathbf{k}}$. This is true when the radius of the scatterers is small compared to the typical wavelength in the system [5], which is an accurate approximation in our experimental setup. We also refer the reader to [5] for an explicit expression of the mean free path $c_0\Sigma^{-1}$ in terms of the statistical properties of the random medium.

The derivation of the radiative transport from wave equation has been addressed extensively in the literature. We refer the interested readers to [20] for a physical point of view and to [3, 1, 19] for more mathematical derivations. Numerical validations of the transport approximation are presented in [5] for frequency domain wave simulations and in [3, 17] for time domain wave simulations.

2.2 Transport-based inclusion reconstruction

The transport-based imaging method proposed in [4, 5] aims to reconstruct extended objects buried in a highly scattering environment using (incoherent) wave energy data instead of wave field data. In this paper, we restrict ourselves to the reconstruction of a single inclusion although the reconstruction of several inclusions is possible from a theoretical viewpoint provided that we have access to sufficiently accurate data. Since the wave energy density solves the phase-space radiative transport equation, the imaging problem can be transformed into an inverse transport problem. We recall that because of the multiple scattering effect of the medium, most of the coherent information regarding the details of the inclusions has been lost. One should thus not expect to reconstruct every detail of the inclusion. Instead, only a few characteristic parameters

of the underline medium and of the embedded inclusions in the medium are accessible. The parameters we consider in this paper are the mean free path of the medium $c_0\Sigma^{-1}$ and the location and size of the inclusion. For the rest of the paper, we assume that the medium is statistically homogeneous inside a rectangle Ω so that Σ is constant in Ω and equal to 0 outside Ω .

We consider in this work the framework where differential measurements are available. This means that we assume the availability of measurements in the presence *and* in the absence of the inclusion. The benefits of differential measurement lie in the fact that the difference between the data with and without inclusion is caused only by the presence of the inclusion. As a result, one can expect to be able to reconstruct inclusions whose influence on the measurements is below the noise level generated by our lack of knowledge of the specific configuration of the medium. However, because we do not know the specific configuration of the medium, we cannot estimate the scattering coefficient Σ in the transport equation (4) in advance. We have to reconstruct this coefficient together with the inclusion's characteristics from available data; see [5] for additional details.

The experiments considered here are based on a three dimensional geometry that is invariant along the vertical axis. As a consequence, we can approximate the experimental data as being two dimensional and thus use a two-dimensional inverse transport theory. Although the methodology generalizes to other shapes, we assume that the inclusions are cylinders parameterized by their central location \mathbf{x} and their radius R .

The transport-based imaging method is done in two steps that we now present in detail. In the first step, we estimate the mean free path of the random medium and in the second step, we reconstruct the parameters characterizing the image.

2.2.1 Step I: reconstructing the scattering coefficient

We use the measured data in the absence of a inclusion to estimate the scattering coefficient of the medium. This is done by solving an inverse transport problem. We want to find a scattering coefficient for the transport equation such that the corresponding solution is as close as possible to the experimental energy measurements. This one-parameter minimization procedure is done numerically. More precisely, the best scattering coefficients, Σ_b , is computed via

$$\Sigma_b = \arg \min_{\Sigma \in \Pi_A} \mathcal{O}(\Sigma), \quad (6)$$

where $\Pi_A = [\Sigma_{min}, \Sigma_{max}]$ is the constraint imposed on the value of Σ , and the mismatch function, often called objective function, is given by

$$\mathcal{O}(\Sigma) = \frac{1}{2} \sum_{j=1}^J |E_m^j - E_p^j|^2, \quad (7)$$

where E_p^j is the transport model prediction at receiver j , and E_m^j is the corresponding wave measurement for the medium in the absence of an inclusion. The minimization technique will be described in more detail below.

2.2.2 Step II: reconstructing extended inclusions

Once Σ has been estimated, two slightly different approaches to reconstructing the parameters of the buried inclusion can be considered. The first approach is better suited to the reconstruction of large inclusions compared to the wavelength. The second approach is preferable for inclusions whose diameter is comparable to or smaller than the wavelength.

Coefficient reconstruction approach. In this approach, inclusions are treated as localized modifications of the scattering coefficient in the transport equation. This allows us to reconstruct two types of inclusions. The first type consists of non-penetrable inclusions, which are treated as having an infinite scattering coefficients. Waves thus reflect specularly at the inclusion's boundary ∂D and the boundary conditions for $\Phi(\mathbf{x}, \hat{\mathbf{k}})$ are thus of the form

$$\Phi(\mathbf{x}, \hat{\mathbf{k}}) = \Phi(\mathbf{x}, \hat{\mathbf{k}} - 2\hat{\mathbf{k}} \cdot \mathbf{n}(\mathbf{x})\mathbf{n}(\mathbf{x})), \quad \mathbf{x} \in \partial D, \quad (8)$$

where $\mathbf{n}(\mathbf{x})$ is the outward unit normal to D at $\mathbf{x} \in \partial D$. The second type of inclusions we consider are void regions, i.e., void/absence of any scatterers. Void regions are modeled by a vanishing scattering coefficient at the transport level.

Our aim is to reconstruct the location (\mathbf{x}) and the radius (R) of such inclusions. The reconstruction is done by solving the following minimization problem:

$$(\mathbf{x}_b, R_b) = \arg \min_{(\mathbf{x}, R) \in \Pi_B} \delta \mathcal{O}(\mathbf{x}, R) \quad (9)$$

where Π_B is the set of constraints imposed on the parameters \mathbf{x} and R and where

$$\delta \mathcal{O}(\mathbf{x}, R) = \frac{1}{2} \sum_{j=1}^J |\delta E_p^j - \delta E_m^j|^2. \quad (10)$$

Here, δE_p^j and δE_m^j correspond to the difference of energies with and without the inclusion for the transport model and the wave data, respectively, at detector j .

Source reconstruction approach. For differential measurement, apart from measurement errors, the difference in the two data sets is caused solely by the presence of the inclusion. The inclusion generates a perturbation in the local energy density field and this perturbation then propagates to the receivers. The propagation of the perturbation follows the radiative transport equation (4). When the inclusion is relatively small, the specular reflection of energy at its boundary is not accurate. Instead, we can treat the inclusion as a point source in the transport equation with an isotropic radiation pattern since the inclusion is assumed to have spherical symmetry. The recovery of the location of the inclusion is equivalent to the recovery of the location of the point source for the transport equation.

The reconstruction of the position of the small inclusion is realized by solving the following minimization problem

$$\mathbf{x}_b = \arg \min_{\mathbf{x} \in \Pi_B} \frac{1}{2} \sum_{j=1}^J \left| \frac{\delta E_p^j - \delta E_m^j}{\delta E_m^j} \right|^2. \quad (11)$$

The above functional is a normalized version of the functional used in (10). The above normalization ensures that the reconstruction depends only on the location of the source term and not on its intensity. Once the inclusion's location is reconstructed, we can presumably use its intensity to infer some properties about the geometry of the inclusion. The relationship between geometry of the inclusion and intensity of the transport source was not investigated in detail in this study.

2.2.3 Numerical minimization

In the above two-step reconstruction method, we need to solve the minimization problems (6), (9) and (11). Let us denote by \mathcal{F} the set of parameters we want to recover. The above minimization problems can be written in a general form as

$$\mathcal{F}_b = \arg \min_{\mathcal{F} \in \Pi} \mathcal{O}(\mathcal{F}). \quad (12)$$

The inversions are done by using a quasi-Newton minimization method which can be characterized by the following iterative process:

$$\mathcal{F}_{k+1} = \mathcal{F}_k + \alpha_k \mathbf{p}_k, \quad (13)$$

where \mathbf{p}_k is a descent direction vector and α_k is the step length determined by a line search method. The descent direction \mathbf{p}_k is the solution of an approximate Newton-type optimality equation, i.e.,

$$\mathbf{p}_k = H_k \mathbf{g}_k, \quad (14)$$

where \mathbf{g}_k is the gradient of the objective function \mathcal{O} with respect to \mathcal{F} , $\mathbf{g}_k = -\nabla_{\mathcal{F}} \mathcal{O}(\mathcal{F}_k)$. H_k is the approximated inverse Hessian matrix of the objective function. We choose a BFGS updating rule

$$H_{k+1} = W_k^T H_k W_k + \rho_k \mathbf{s}_k \mathbf{s}_k^T \quad (15)$$

with $W_k = \mathbf{I} - \rho_k \mathbf{y}_k \mathbf{s}_k^T$, $\mathbf{s}_k = \mathcal{F}_{k+1} - \mathcal{F}_k$, $\mathbf{y}_k = \mathbf{g}_{k+1} - \mathbf{g}_k$, $\rho_k = \frac{1}{\mathbf{y}_k^T \mathbf{s}_k}$, and \mathbf{I} is the identity matrix. We refer the interested reader to [13, 16] for details on the quasi-Newton method with BFGS update rule and [18] for application of the method in inverse transport problems.

2.2.4 Monte Carlo transport solver

In each BFGS iteration, a transport equation has to be solved to evaluate the objective function and to compute the gradient of the objective function with respect to the parameters needed to be reconstructed. We solve the transport equation with the Monte Carlo method [21]. We run enough particles to ensure that the statistical error in the simulation is small enough. We also use the variance reduction technique introduced in [3] to express the difference of energies δE_m^j as the expectation of an appropriate process rather than the difference of two expectations. This allows us to solve the transport equation in the presence of small inclusions at an affordable computational cost.

The aforementioned transport-based reconstruction methods have been shown to perform well with synthetic data; see [5]. The objective of this paper is to validate the inversion technique from experimental electromagnetic (microwave) measurements.

3 Experimental Configuration and Measurements

Electromagnetic scattering measurements have been performed, in a configuration designed to be highly scattering and approximate a two-dimensional system. Specifically, as depicted in Fig. 1, we have employed 600 low-loss dielectric rods (plexiglass). The

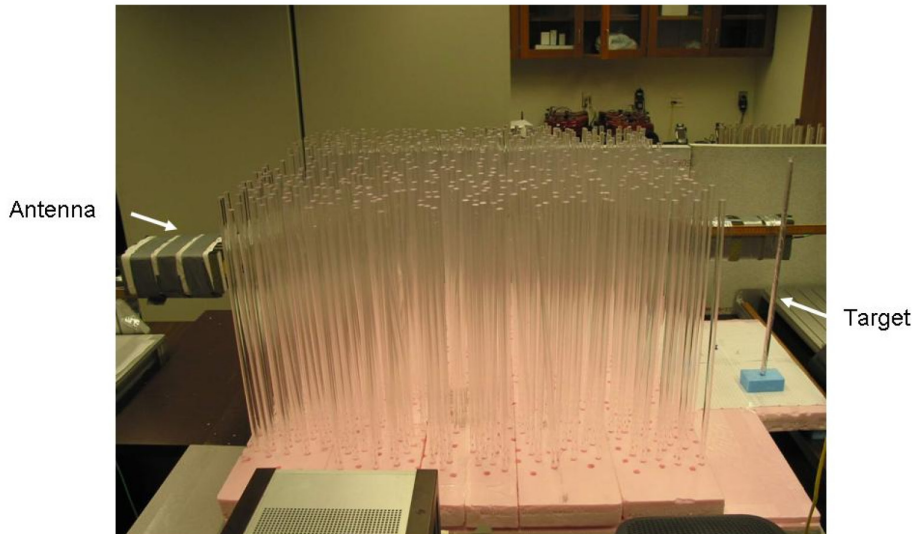


Figure 1: Experimental setting

rods are of 1.25 cm diameter, 0.6 m length, and with approximate dielectric constant $\epsilon_r = 2.5$; the rods were distributed in a random manner (with no particular distribution, although the average inter-rod spacing was 4.5 cm, between rod axes). The rods are situated in a domain 1.0 m long and 1.2 m wide, embedded at the bottom in Styrofoam (the latter with electrical characteristics close to those in free space).

An N-element linear sensor array is placed on one side of the random media, with inter-element spacing 2cm. The antennas are placed at a height that bisects the mid-point of the rods, and the measurements are therefore approximately two-dimensional. The elements of the array are identical Vivaldi antennas and measurements were performed over the 0.5-20 GHz band, with the electric fields vertically polarized (electric fields parallel to the rod axes). The measurements are performed with a vector network analyzer. Such that the scattering physics was in the diffusive regime, the results presented below are based on data averaged over the frequency band [9GHz-11GHz]. We have tested reconstructions based on other similar frequency bands, with similar results. We want to emphasize in this paper that the inverse transport algorithm works in the narrow-band regime and thus will present reconstructions based on measurements in the frequency band [9GHz-11GHz]. Further details on the experimental setup are described in [15].

4 Imaging Results from Experimental Data

We perform here a detailed analysis of the transport-based inversion method based on experimental data obtained in the configuration described in the preceding section.

4.1 Simulation setup

The geometry of the experimental setup is reproduced in our numerical simulation of the inverse transport algorithm. The domain used in the numerical simulations is illustrated in Fig. 2. The region with dots denotes the random media consisting of

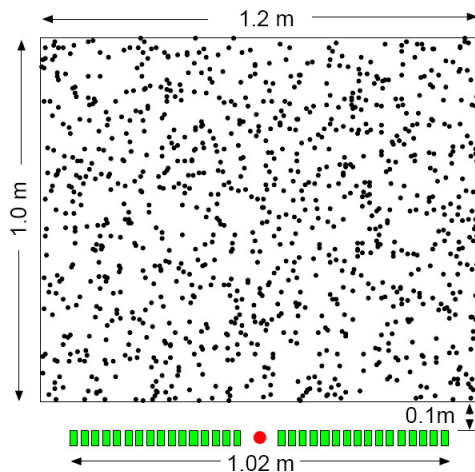


Figure 2: Setup for numerical simulations. Red dot and green squares denote transmitter and receivers, respectively. The separation between two neighboring receivers is 3cm.

localized rods in the experiment. The dimensions of the domain are exactly as in the physical experiments. We associate Cartesian coordinates with the configuration in Fig. 2 where the transmitter is located at the origin (0 cm, 0 cm). The coordinates appearing in the following sections are in Cartesian coordinates.

We note that a two-dimensional setting is most appropriate to model the experimental measurements described in the preceding section. The inverse transport code and its Monte Carlo component are however independent of spatial dimension and work equally well in a three dimensional setting.

The first step in the two-step reconstruction procedure presented in Section 2 consists of estimating the scattering coefficient of the random medium, or equivalently the mean free path $c\Sigma^{-1}$. The best fit Σ_b obtained by solving the minimization problem (6) is equal to 42cm for the frequencies averaged in the band [9GHz-11GHz]. The mean free path is therefore of comparable size though smaller than the overall size of the domain and is significantly larger than the wavelength $\lambda \approx 3\text{cm}$. In most of the experiments presented below, twice the distance from the inclusion to the radiating source is therefore relatively large compared to the mean free path, which is a confirmation that our experimental measurements are well within the radiative transfer regime. Note that the inclusions outside of the random medium are separated by at least 2.5 mean free paths from the radiating source. The coherent signal leaving the radiating source, hitting the inclusion, and returning to the array of detectors therefore propagates through the random medium for at least 5 mean free paths. Its intensity is therefore attenuated by an amount at least equal to $e^{-5} \approx 7 \cdot 10^{-3}$. This means that the intensity of the coherent field is less than 1% of what it would be if propagation occurred in a homogeneous medium and is certainly much smaller than the amount of incoherent energy reaching the detectors. In such situations, inversion methods based on the coherent signal are unlikely to perform

well. We present below what we obtain with the transport-based inversion method.

The mean free path obtained by solving (6) using the frequencies in the band [6.5GHz-8.5GHz] is equal to 91cm. Since scattering increases with frequency, we may expect that the measured scattered field has higher intensity at 8.5GHz than at 6.5GHz. Assume therefore that 91cm is the mean free path at frequency 8.5GHz and that 42cm is the mean free path at frequency 11GHz. Theoretical considerations show that the mean free path decreases like ω^{d+1} for random media with localized scatterers, where d is dimension [5]; this is Rayleigh scattering. For $d = 2$, we find that

$$42\text{cm} \times \left(\frac{11\text{GHz}}{8.5\text{GHz}}\right)^3 \approx 91.03\text{cm}.$$

The best estimates for the mean free paths obtained in (6) based on our experimental results verify the Rayleigh scattering cubic law quite remarkably, which further justifies that we use a two-dimensional setting in our reconstructions.

4.2 Reconstruction of inclusions outside of the random media

We first analyze the case of inclusions located outside of the random media and separated from the source and receivers by a layer of random media. We have performed experiments with inclusions of different sizes and located at different places.

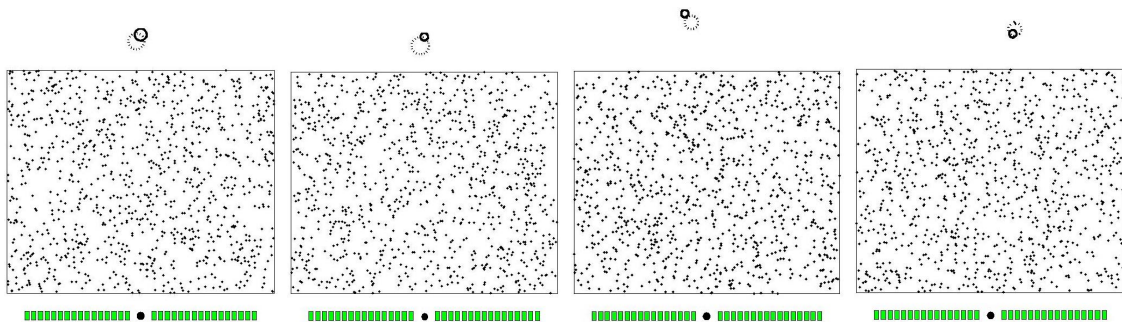


Figure 3: Reconstructions of inclusions with different sizes and locations. Solid and dash-dotted circles denote real and reconstructed inclusions, respectively.

The real and reconstructed locations and radii of the inclusions are summarized in Tab. 1 for six different experiments and for the two inverse transport methods described in Section 2. We show in Fig. 3 four typical reconstructions. We observe that the reconstructions agree well with the real parameters for most of the experiments. The locations of the inclusions are well-captured by both the coefficient reconstruction procedure and the source reconstruction procedure. The sizes of the inclusions are still captured satisfactorily though not as well as the locations. We observe that both methods fail to reconstruct the smallest object considered in the experiment. The most likely explanation is that the object falls below the noise level of our experimental setting.

4.3 Reconstructing void regions

In the next set of experiments, we remove three nearby rods from the random medium and aim at reconstructing the location of the missing rods. We model the missing rods

	Real		Reconstruction ^a		Reconstruction ^b
	location	radius	location	radius	location
Experiment 1	(0, 136)	2.75	(-2.1, 123.3)	3.65	(-1.3, 120.1)
Experiment 2	(10, 126)	1.75	(11.2, 127.9)	2.98	(8.9, 125.2)
Experiment 3	(0, 126)	1.75	(2.1, 122.3)	2.46	(3.3, 120.0)
Experiment 4	(0, 136)	1.75	(2.0, 130.4)	3.54	(-1.2, 132.7)
Experiment 5	(-10, 136)	1.75	(-6.7, 132.0)	3.10	(-6.4, 129.4)
Experiment 6	(0, 136)	0.75	fail	fail	fail

Table 1: Reconstructed locations and radii for six different experiments. Units are in centimeters. ^aReconstruction done with the coefficient reconstruction method; ^bReconstruction done with the source reconstruction method.

as a void and do not try to reconstruct the rods individually. Four sets of experiments have been performed. We plot the results for the reconstructions in Fig. 4. The locations

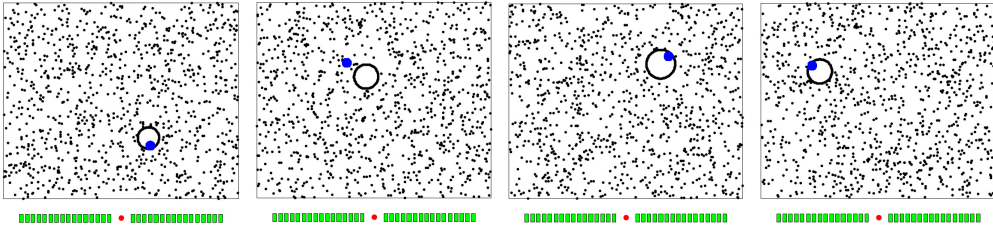


Figure 4: Reconstructions of void regions made by removing three nearby rods. Blue points in the media denote centers of the holes.

and effective radii of the voids are summarized in Tab. 2. As described in the previous section, we have a total number of 600 rods occupying a domain of area 1.2 square meters. Thus on average, 3 rods occupy a total area of 0.006 square meters. This means that if we assume the region occupied by the 3 rods is circular, we will have a void region of radius roughly 4.5 cms. The reconstruction of the void regions is thus reasonably good.

	Real		Reconstruction	
	location	radius ^a	location	radius
Experiment 1	(15, 37)	4.5	(13.6, 40.8)	5.5
Experiment 2	(-14, 79)	4.5	(-4.3, 72.4)	6.4
Experiment 3	(22, 83)	4.5	(18.3, 78.6)	7.4
Experiment 4	(-34, 78)	4.5	(-30.4, 72.5)	6.2

Table 2: Reconstructed locations and radii form six different experiments. ^aRadius is an approximated value estimated from the experimental configuration. All numbers are in centimeters.

4.4 Reconstructing small inclusions

To see how well we can reconstruct small inclusions, we performed experiments with inclusion of radius 0.75 cm. The radius of the rods in the background medium have a radius of 1.25 cm, so that the radius of inclusion is significantly smaller than that of the rods. Since the inclusions are quite small, the inverse point source method is used in the reconstruction. Only the location of the inclusion is sought. We have not considered any model relating its size to its scattering strength. We show in Fig. 5 two results obtained

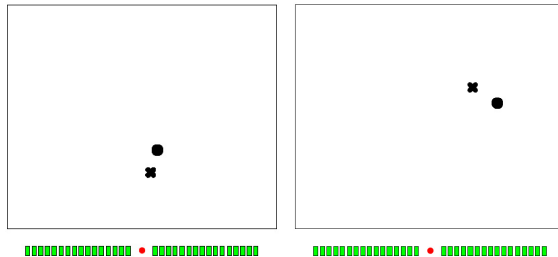


Figure 5: Reconstruction of a small inclusion buried inside the media. The dot and the cross denote the real and reconstructed inclusions, respectively. The background medium is not shown to improve readability.

from the experimental data. In the first experiment, the inclusion is located at (7cm, 45cm) and the reconstructed location is (4cm, 35cm). In the second experiment, the real location of the inclusion is (30cm, 66cm) and the reconstructed location is (19cm, 73cm). In both cases, the reconstructions are not as good as the ones obtained in the preceding sections. An explanation for this inaccuracy is that the noise in the experimental measurements is relatively high compared to the influence of the inclusion on the measurements. As we have emphasized above, differential measurements eliminate the noise coming from our lack of knowledge of the random medium. However, differential measurements do not eliminate instrumental noise in the measurements, and we believe that such a noise is the limiting factor in the reconstructions.

4.5 Reconstructing an inclusion behind a blocker

One of the main advantages of transport-based imaging methods is that they can image inclusions hidden behind blockers. Since the line of sight is blocked, traditional methods based on coherent wave data fail to image the inclusion. The incoherent scattering effects from the random medium do help in this case. Because of multiple scattering, the influence of the inclusion can propagate around the blocker and reach the receivers. To a certain extent, multiple scattering increases the effective “aperture” of the receivers.

We now consider the reconstruction of an object hidden behind a locker. In the experiment, a round blocker with radius 15 cm is placed at (7cm, 55cm). A small object with radius 1.75cm is placed behind the blocker. The exact location of the inclusion is (7cm, 76cm). The reconstructed result is shown in Fig. 6. The reconstructed center of the inclusion is (10cm, 86cm). Although it is not perfect, the reconstruction is still satisfactory given that the inclusion is relatively small.

We emphasize that the reconstruction of a inclusion hidden behind a blocker is impossible from coherent wave measurements. Inverse transport however is mostly

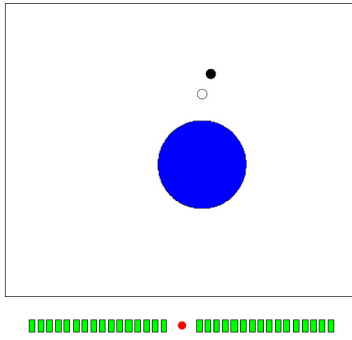


Figure 6: Reconstruction of a inclusion hidden behind a blocker (big circle). The circle and the dot in the domain denote the real and reconstructed inclusions, respectively. The background medium is not shown to improve readability.

insensitive to the presence of the blocker, provided that multiple scattering is sufficiently strong and statistically stable.

5 Conclusions and Remarks

We have conducted a series of experimental studies on the problem of imaging in highly scattering environment. We have demonstrated the performance of the transport-based imaging method in practical situations.

Our experiments cover a variety of practical geometries: inclusions buried inside a random medium, separated from the source and detectors by a layer of random media, or hidden from the sources and detectors by a large object blocking line of sight measurements. In all cases where the inclusion was sufficiently large, the reconstructions based on the transport-based imaging method were quite satisfactory. Our study shows that the method can be used for imaging in random media in situations where multiple scattering effects are so significant that inversions based on coherent-wave information cannot work.

Acknowledgment

This work was supported in part by DARPA-ONR grant N00014-04-1-0224 and NSF Grant DMS-0239097. GB also acknowledges support from the Alfred P. Sloan Fellowship.

References

- [1] G. BAL, G. PAPANICOLAOU, AND L. RYZHIK, *Radiative transport limit for the random Schrödinger equation*, *Nonlinearity*, 15 (2002), pp. 513–529.
- [2] G. BAL AND O. PINAUD, *Time-reversal based detection in random media*, *Inverse Probl.*, 21 (2005), pp. 1593–1620.

- [3] ———, *Accuracy of transport models for waves in random media*, Wave Motion, 43 (2006).
- [4] ———, *Kinetic models for imaging in random media*. Preprint, 2007.
- [5] G. BAL AND K. REN, *Transport-based imaging in discrete random media*. Preprint, 2007. Available at:
<http://www.columbia.edu/~gb2030/PAPERS/TransportFrequency.pdf>
- [6] B. BORCEA, G. PAPANICOLAOU, AND C. TSOGKA, *Theory and applications of time reversal and interferometric imaging*, Inverse Probl., 19 (2003), pp. S139–S164.
- [7] L. BORCEA, G. PAPANICOLAOU, AND C. TSOGKA, *Interferometric array imaging in clutter*, Inverse Probl., 21 (2005), pp. 1419–1460.
- [8] ———, *Adaptive interferometric imaging in clutter and optimal illumination*, Inverse Probl., 22 (2006), pp. 1405–1436.
- [9] T.-K. CHAN, Y. KUGA, AND A. ISHIMARU, *Experimental studies on circular SAR imaging in clutter using angular correlation function technique*, IEEE Trans. Geosci. Remote Sensing, 37 (1999), pp. 2192–2197.
- [10] M. CHENEY AND R. J. BONNEAU, *Imaging that exploits multipath scattering from point scatters*, Inverse Probl., 20 (2004), pp. 1691–1711.
- [11] A. J. DEVANEY, E. A. MARENGO, AND F. K. GRUBER, *Time-reversal-based imaging and inverse scattering of multiply scattering point targets*, J. Acoust. Soc. Am., 118 (2005), pp. 3129–3138.
- [12] F. K. GRUBER, E. A. MARENGO, AND A. J. DEVANEY, *Time-reversal imaging with multiple signal classification considering multiple scattering between the targets*, J. Acoust. Soc. Am., 115 (2004), pp. 3042–3047.
- [13] C. T. KELLEY, *Iterative Methods for Optimization*, Frontiers in Applied Mathematics, Society of Industrial and Applied Mathematics, Philadelphia, 1999.
- [14] D. LIU, G. KANG, L. LI, Y. CHEN, S. VASUDEVAN, W. JOINES, Q. H. LIU, J. KROLIK, AND L. CARIN, *Electromagnetic time-reversal imaging of a target in a cluttered environment*, IEEE Trans. Antenna Propag., 53 (2005), pp. 3508–3566.
- [15] D. LIU, S. VASUDEVAN, J. KROLIK, G. BAL, AND L. CARIN, *Electromagnetic time-reversal imaging in changing media: Experiment and analysis*, IEEE Trans. Antenna Propag., 55 (2007), pp. 344–354.
- [16] J. NOCEDAL AND S. J. WRIGHT, *Numerical Optimization*, Springer-Verlag, New York, 1999.
- [17] J. PRZYBILLA, M. KORN, AND U. WEGLER, *Radiative transfer of elastic waves versus finite difference simulations in two-dimensional random media*, J. Geophys. Res., 111 (2006). B04305.

- [18] K. REN, G. BAL, AND A. H. HIELSCHER, *Frequency domain optical tomography based on the equation of radiative transfer*, SIAM J. Sci. Comput., 28 (2006), pp. 1463–1489.
- [19] L. RYZHIK, G. PAPANICOLAOU, AND J. B. KELLER, *Transport equations for elastic and other waves in random media*, Wave Motion, 24 (1996), pp. 327–370.
- [20] P. SHENG, *Introduction to Wave Scattering, Localization, and Mesoscopic Phenomena*, Academic Press, San Diego, CA, 1995.
- [21] J. SPANIER AND E. M. GELBARD, *Monte Carlo Principles and Neutron Transport Problems*, Addison-Wesley, Reading, Mass., 1969.
- [22] G. ZHANG AND L. TSENG, *Application of angular correlation function of clutter scattering and correlation imaging in target detection*, IEEE Trans. Geosci. Remote Sensing, 36 (1998), pp. 1485–1493.